



# Synthesis and characterization of copper-nanocarbon films with enhanced stability



Romaine A. Isaacs<sup>a</sup>, H.M. Iftexhar Jaim<sup>a</sup>, Daniel P. Cole<sup>b</sup>, Karen Gaskell<sup>c</sup>, Oded Rabin<sup>a,d</sup>, Lourdes G. Salamanca-Riba<sup>a,\*</sup>

<sup>a</sup> Department of Materials Science and Engineering, University of Maryland, College Park, MD, USA

<sup>b</sup> Army Research Laboratory, Aberdeen Proving Ground, Adelphi, MD, USA

<sup>c</sup> Department of Chemistry and Biochemistry, University of Maryland, College Park, MD, USA

<sup>d</sup> Institute for Research in Electronics and Applied Physics, University of Maryland, College Park, MD, USA

## ARTICLE INFO

### Article history:

Received 21 March 2017

Received in revised form

30 May 2017

Accepted 19 June 2017

Available online 21 June 2017

### Keywords:

Copper

Carbon

Covetics

Transparent

Electrode

## ABSTRACT

Copper-nanocarbon, called covetic, films made using pulsed laser deposition (PLD) from a target containing nominally 4 wt% carbon in the copper matrix show uniform integration of up to  $4.1 \pm 0.2$  wt.% C. We observe evidence of  $sp^2$  carbon in PLD Cu covetic films in XPS and a peak in the C K-edge in electron energy loss spectroscopy indicative of transitions from the 1s to  $\pi^*$  anti-bonding unoccupied state, suggesting that the C incorporated in the film is graphitic in nature. We measure sheet resistance of 1.7 Ohm/sq and transmittance of 25% at 550 nm in a  $\approx 27$  nm thick PLD Cu covetic film after deposition. These films also show much reduced oxidation by scanning probe techniques and very stable resistance for over 120 days - significantly longer than e-beam films of the same thickness. Cu covetic films made by PLD show good promise as transparent electrodes.

© 2017 Elsevier Ltd. All rights reserved.

## 1. Introduction

Copper (Cu) has been an industry standard in many electrical and thermal applications, such as bonding wires and as interconnects, but many problems persist and as such has been a topic of considerable interest for some time [1–3]. More recently, Cu is being used as a transparent electrode in optoelectronic devices such as organic solar cells, flexible OLED displays, and in touch screen applications [4–6]. In each of these devices the electrode must be transparent and be able to transport electrons away from the active layer. One primary challenge for using Cu in nano-electronics is its tendency to oxidize in  $O_2$ -rich environments; this leads to the formation of an oxide layer comprised of CuO and  $Cu_2O$ , which can quickly diminish the conductivity of the metal [7]. In microprocessors, Cu interconnects supply power to the various components in integrated circuits, but are generally embedded below the surface to prevent oxidation [8]. In optoelectronic devices, Cu is attractive because it is abundant and cheaper than ITO [9]. However, both in microprocessors and optoelectronic devices,

more flexibility could be achieved if the oxidation of copper could be slowed, or preferably prevented.

The oxidation of Cu can be reduced through passivation [5,8,10]. One approach to Cu passivation is the incorporation of graphitic carbon into the structure of Cu. Graphene on Cu surfaces has been shown to be an impenetrable barrier to oxygen [11]. Graphene [12–14] and CNTs [15–17] have also been considered in nano-electronics because of their high electrical and thermal conductivities. Incorporating C in the Cu host lattice could improve electrical conductivity of the combined product given the superior performance of graphitic nanostructures, when compared to Cu. Some reported structures are promising but require a sandwich [18], or two-step process [4], where fabrication of the active layer occurs in one step and then transferred to a transparent substrate. This makes commercialization of transparent conducting electrodes using these techniques challenging, so different approaches are still being investigated.

Until recently [19], attempts to combine C with Cu have been quite limited due to the low solubility of C in Cu [20]. In our previous work, we demonstrated transparent conducting films made from Cu covetic, but with low C concentration (<0.1 at.%) [21]. In order to investigate the effect of higher C content we deposited

\* Corresponding author.

E-mail address: [riba@umd.edu](mailto:riba@umd.edu) (L.G. Salamanca-Riba).

**Table 1**  
Deposition conditions used for Cu cv 4% films using PLD.

Film Conditions	Laser Power (W)	Substrate Temp (C)	Deposition Time (mins)	Film Thickness (nm)	C concentration from XPS <sup>a</sup> (at.)/(wt.%)
1	1.93	150	15	10	no C
2	3.55	150	20	11	no C
3	3.2	150	60	13	seg. C
4	2.4	150	60	10	2.62/0.44
5	3.3	350	64	20	no C
6	2.6	500	60	21	5.20/1.1
7	2.0	500	120	27	19.14/4.1

<sup>a</sup> Based on carbon and copper only, oxygen excluded from calculation.

copper covetic films using pulsed laser deposition (PLD). PLD is known to transfer ions, molecules and larger structures in the ablation process. As such, we sought to employ this method to transfer graphitic structures embedded in the Cu lattice of a bulk Cu covetic target into thin films. Using PLD we were able to transfer Cu and C simultaneously in a one step process onto a substrate. Films were deposited on Si (100), and sapphire ( $\alpha$ -Al<sub>2</sub>O<sub>3</sub>) (11 $\bar{2}$ 0) substrates using a Cu covetic target with a nominal C concentration of 4 wt% (denoted Cu cv 4%). The laser power, substrate temperature and deposition time were tuned to achieve a conducting, optically transparent film. In this paper we present a detailed analysis of the synthesis, characterization and properties of Cu cv 4% films made by PLD and report that graphitic carbon is uniformly dispersed in a polycrystalline Cu film. Furthermore, these films show reduced oxidation and improved electrical stability over time.

## 2. Results and discussion

PLD of copper, under similar conditions as described here, has been previously studied in great detail [22]. In order to produce a transparent conducting film from the copper covetic bulk, the optimum photoablation parameters must be ascertained to ensure that the carbon structures are transferred from the target to the film. The substrate temperature and laser power also influence the structure and properties of the film. Cu covetic is comprised of Cu and C, where each element has a different interaction with the laser beam and can give rise to preferential sputtering of one element over the other. In order to produce a homogeneous film, the deposition parameters were altered and the resulting structure of the films analyzed. Spectroscopy techniques such as x-ray diffraction (XRD), x-ray photoelectron spectroscopy (XPS), energy

dispersive x-ray spectroscopy (EDS) and electron energy loss spectroscopy (EELS) as well as microscopy techniques such as atomic force microscopy (AFM), conductive AFM (C-AFM), and transmission electron microscopy (TEM) were used to characterize the PLD films. 4 point-probe and UV-VIS spectroscopy were used to investigate the electrical and optical properties, respectively. Table 1 presents a sample of the PLD films in this study with corresponding photoablation parameters. All films were grown in 100 mTorr of 99.999% Argon. PLD films (1–6) were grown on Si(100) substrates, while film (7) was simultaneously deposited on Si(111) and Sapphire ( $\alpha$ -Al<sub>2</sub>O<sub>3</sub>). Films of pure copper were also grown by PLD under the same conditions for comparison.

In our previous work, we showed that a 30 nm thick Cu covetic film made by e-beam deposition exhibited a sheet resistance of 2 Ohm/sq and 28% transmittance at 550 nm [21]. We attempted to improve these optoelectronic properties by increasing the carbon concentration in the deposited films using PLD. Films 1–4 in Table 1 were deposited at a constant temperature of 150 °C in order to optimize the laser power, while films 5–7 demonstrate the effect of temperature. XRD spectra from films (2)–(7) are shown in Fig. 1(a). Films 1, 2, 3 and 5, produced with laser powers >3 W or <2 W are not uniformly metallic films. At these laser powers Cu was preferentially sputtered from the target, and was soon oxidized to Cu<sub>2</sub>O. In films = 3, C is sputtered first, but is segregated from the Cu layer. Film 4, while homogeneous in composition (by XPS), was mostly amorphous (by selected area electron diffraction in TEM) and along with film (5), which was completely amorphous, exhibited high electrical resistivity (20 M Ohms). In contrast, film (6) deposited on Si (100) and film (7) deposited simultaneously on Si (111) and sapphire were both fabricated at laser powers between 2 and 3 W and at high temperature (500 °C). Both films show strong Bragg peaks at  $2\theta = 44$  and  $52^\circ$  corresponding to Cu (111) and (200) reflections, respectively, without evidence of any oxide phases. They demonstrate that we were able to produce homogeneous crystalline films with uniform carbon content throughout the film thickness and independent of the substrate material. Films 2, 4 and 5 do not have significant Bragg peaks. However, for the polycrystalline films we can calculate the grain size listed in Table 2 from the Cu (111) and Cu (200) peaks using the Scherrer equation:  $\tau = k\lambda/\beta\cos(\theta)$ , where,  $\tau$  is the mean grain size,  $k$  is a dimensionless shape factor with a typical value of about 0.9,  $\lambda$  is the X-ray wavelength,  $\beta$  is the FWHM of the peak and  $\theta$  is the Bragg angle (in degrees).

XPS depth profile from film (7) on Si substrate, shown in Fig. 1(b), measured an average C content of 4.1 wt% (19.14 at.%) in

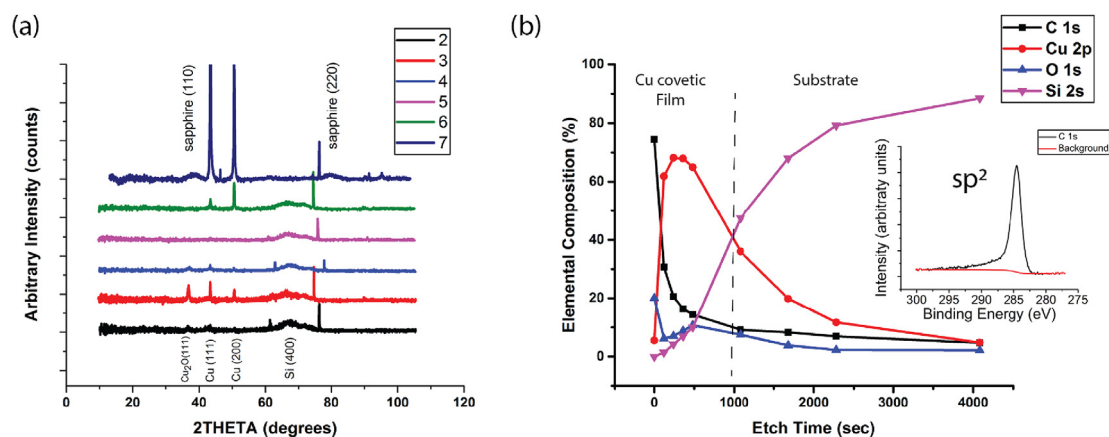


**Fig. 1.** (a) X-ray diffraction of the Cu cv 4% films grown via PLD described in Table 1, (b) XPS of film (7) on Si(111) substrate showing an average of 4.1 wt% (19.14 at.%) C concentration in the film region, with the inset showing the C 1s peak after 240 s of sputtering. (A colour version of this figure can be viewed online.)

**Table 2**

Mean grain size of polycrystalline Cu covetic films calculated using (111) and (200) reflections.

Film	Reflections	
	(111)	(200)
	(nm)	
3	54	42
6	36	44
7	37	37

the film region. Oxygen and adventitious surface hydrocarbon were excluded from the at.% calculation for consistency across samples. The increase in oxygen seen before the film-substrate interface (marked with dashed line) is due to a small amount of native oxide ( $\text{SiO}_2$ ) on the surface of the substrate. The interface is not sharp due to Cu diffusion into the Si substrate [23]. The sputtering rate of Cu,  $\text{SiO}_2$  and C was measured to be 10.2 nm/min, 5 nm/min and 2.7 nm/min, respectively. When Cu is calibrated to 932.6 eV, the adventitious hydrocarbon on the surface sits at 284.9 eV. Upon sputtering, the adventitious hydrocarbon is removed in the first sputter cycle and the C 1s peak shifts to 0.5 eV lower binding energy (284.5 eV) with an asymmetric tail to higher binding energy characteristic of  $sp^2$  carbon as seen in the C 1s spectrum (inset to Fig. 1(b)) after 240 s of sputtering.

A Cu metal film and a Cu covetic film, were grown using the same PLD film conditions (6) within 24 h of each other. Immediately after deposition, the grain sizes of both samples were uniform and the roughness of both samples was  $\approx 1.5$  nm as determined from AFM images (not shown). However, differences between their morphology can be clearly seen in AFM images taken 28 and 34 days after deposition for the Cu metal and Cu covetic films respectively (Fig. 2). From the phase contrast images it is evident that the Cu covetic film is homogeneous, while the Cu metal film shows regions of high contrast where the film has oxidized. No such oxidation is evident in the covetic film over approximately the same time period. The mechanism for oxidation is controlled by grain boundary diffusion, where Cu is oxidized first to  $\text{Cu}_2\text{O}$  and

then to  $\text{CuO}$  [10,24,25]. In the case of the Cu covetic film, the presence of carbon in the structure seems to have effectively reduced the onset of oxidation. This effect can be seen in a comparison of high resolution XPS spectra of the two films shown in Fig. 3. The Cu  $2p^{3/2}$  peak is located at binding energy of 932.7 eV with spin orbit splitting of 19.75 eV corresponding to Cu  $2p^{1/2}$ . Oxide peaks (for Cu bonded to O) appear at  $\approx 943$  eV as a collection of satellite peaks. The Cu covetic sample clearly demonstrates reduced oxidation compared to the Cu film.

Conductive Atomic Force Microscopy (C-AFM) was used to investigate the local electrical properties of the Cu metal and Cu covetic films (Fig. 2). C-AFM scans were performed in contact mode with solid Pt probes ( $k_s \sim 8$  N/m,  $R_c \sim 20$  nm) on both pure Cu and Cu covetic films using a similar sample bias. The Cu covetic film displayed a much more uniform local conductivity compared to the Cu metal, which is attributed to the enhanced stability. Alternatively, the Cu metal showed local spikes of high conductivity (higher than the covetic film at particular points), but overall displayed a lower local conductivity than the covetic film, likely due to the increased oxidation.

A TEM lamella was fabricated from film (6) (Fig. 4). The  $\approx 20$  nm Cu cv 4% film deposited on a Si (100) substrate and covered with a Pt protection layer exhibits a continuous film with RMS roughness of  $\approx 4$  nm in agreement with the value measured by AFM. EELS from the Cu cv 4% film (6) was acquired in scanning TEM mode (STEM) using a JEOL high angle annular dark field (HAADF) detector. Fig. 5(a) shows a HAADF image consisting of the substrate with dark and Pt with bright contrast. The region analyzed is demarcated with the green box and includes the film, as well as thin areas of the substrate and Pt layer. A higher resolution image of this region is shown in the HAADF image in Fig. 5(b). The C K-edge spectrum image acquired using a spot size of 1.5 nm, dwell time of 0.05 s and dispersion of 0.3 eV/channel is shown in Fig. 5(c). At each pixel in the image a spectrum is acquired. The total spectrum of the film layer indicated in the red rectangle of Fig. 5(c) is shown in Fig. 5(d), where the background signal has been subtracted to reveal the intensity corresponding to the C K-edge. This signal is weak due in part to the short dwell time used in order to minimize contamination during data acquisition and also because of the low carbon

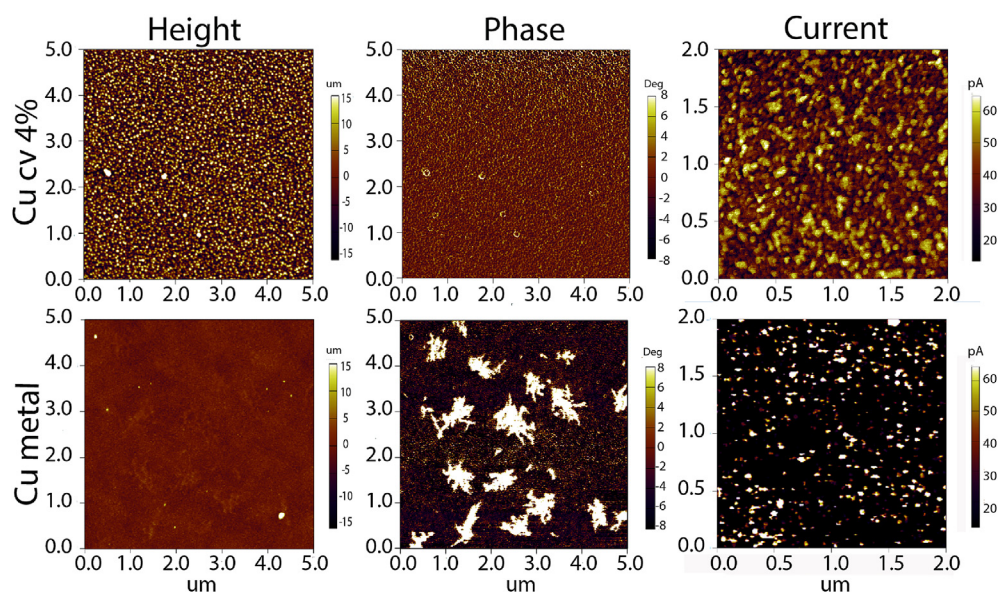


**Fig. 2.** AFM images comparing the grain structure in the height image ( $5 \mu\text{m} \times 5 \mu\text{m}$ , left column) the phase contrast ( $5 \mu\text{m} \times 5 \mu\text{m}$ , center column) and Conductive AFM images ( $2 \mu\text{m} \times 2 \mu\text{m}$ , right column) mapping the local electrical conductivity of Cu covetic (top row) and Cu metal (bottom row) samples. (A colour version of this figure can be viewed online.)

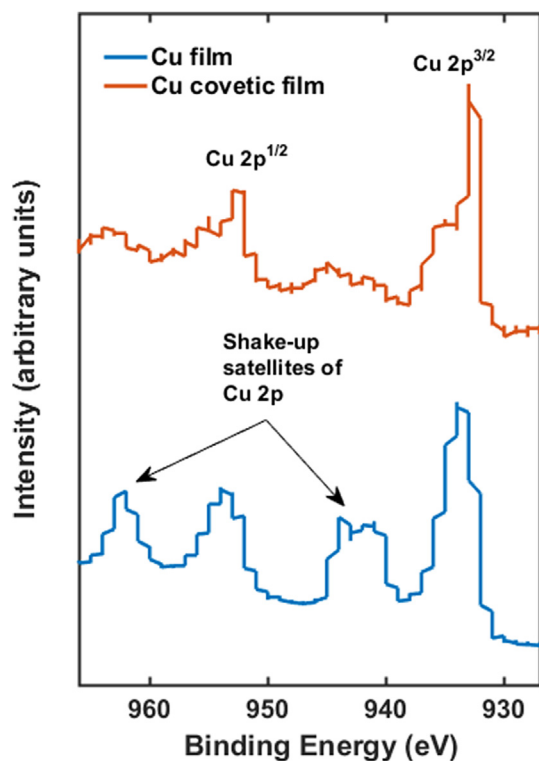


**Fig. 3.** High Resolution XPS of Cu 2p spectrum demonstrating reduced oxidation in Cu covetic film compared to pure Cu. (A colour version of this figure can be viewed online.)

content in the film. Nevertheless, it shows the presence of C in this region that gives rise to spots in microdiffraction patterns (not shown) with interplanar d-spacing of 0.348 nm corresponding to (002) of graphite. Fig. 5(e) shows a map of the C K-edge from this region clearly indicating the presence of C within the film layer, which a line profile (Fig. 5(f)) indicates is neither present in the substrate or Pt protection layer. Thus, carbon in the Cu covetic target can be transferred to the film by PLD within a narrow range of growth parameters.

We analyzed the EELS spectrum images using the multivariate analysis method (MVA). In this approach, EELS spectra can be described via a parametric model as composed of a finite number of components and noise. The Hyperspy Python library provides convenient access to the most commonly used MVA decomposition algorithms including principal component analysis (PCA) and Blind

Source Separation (BSS) [26]. BSS has been used to analyze the EELS spectra taken from materials that have elements with overlapping edges [27]. We used PCA to find the minimum number of components that define our dataset and BSS to map the components, elucidate the fine structure of the C K-edge in Cu covetic samples, and to distinguish between adventitious hydrocarbon (contamination) and incorporated carbon in the films. The EELS spectra of film (6) were decomposed into three components that could be easily identified, as shown in Fig. 6: carbon (Covetic) that is found in the film region of the sample, the background, and C contamination. Carbon in the film region has a rise at  $\approx 284$  eV where the carbon K-edge is located and shows a fairly uniform intensity indicating uniform distribution of carbon within the film region. The intensity in the background region is uniform throughout the area mapped and hydrocarbon contamination can be distinguished from C in covetic by the shape of the edge in the signal space, which should be similar to the carbon signal but without a defined  $sp^2$  or  $sp^3$  peak. This MVA of the EELS spectrum image not only reproduces the result obtained from the background subtraction in Fig. 5(d), but also gives more detailed information about the fine structure of the C K-edge. Namely, there is some  $sp^2$  character as evidenced by the weak edge at 285 eV, indicating transitions from the 1s occupied state to the  $\pi^*$  unoccupied states. However, the dominant feature is the edge at 290 eV, indicating transitions from 1s occupied state to the  $\sigma^*$  unoccupied states, which is observed in both  $sp^2$  and  $sp^3$  C.

In order to measure the optical properties of Cu cv 4% films, we deposited film (7) with the same photoablation parameters as film (6) on an insulating, transparent crystalline substrate - A-plane sapphire (11 $\bar{2}$ 0) since sapphire has 99.4% transmittance over the studied wavelength range of 300–1100 nm. Film (7) was  $\approx 27$  nm thick and exhibited transmittance of 25% at 550 nm. This is notably lower than a Cu cv 5% film of approximately the same thickness made by e-beam deposition (28% at 550 nm) on sapphire (Fig. 7(a)). 4-point probe resistivity measurements were made to determine the sheet resistance using the Van der Pauw method. After deposition, the sheet resistance of film (7) was 1.7 Ohm/sq, but as expected this increased with time. We performed a longitudinal study, measuring the sheet resistance over time, as a method to elucidate the film's resistance to oxidation as shown in Fig. 7(b). It is clear that over the period tested the PLD film is significantly more stable than the Cu cv 5% film of the same thickness made by e-beam deposition. This is likely due to the higher concentration of carbon incorporation in the PLD film (19.14 at.%) compared to the e-beam film (<0.1 at.%). The sheet resistance of the PLD film increased by only  $\approx 9$  Ohm/sq over 130 days indicating that carbon increases the resistance to oxidation of the Cu covetic films.

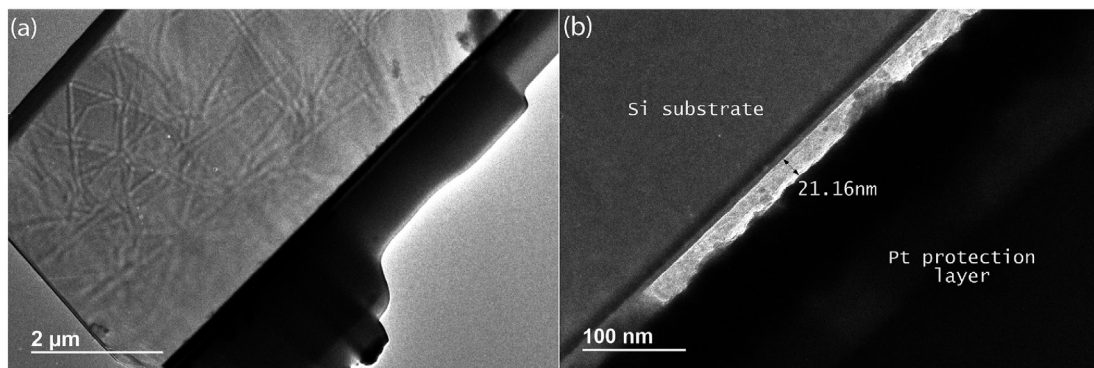


**Fig. 4.** TEM images: (a) Low resolution image of cross section lamella made using FIB, (b) Higher magnification image of the Cu cv 4% PLD (6) film measuring 21.16 nm on Si (100) with Pt protection layer.

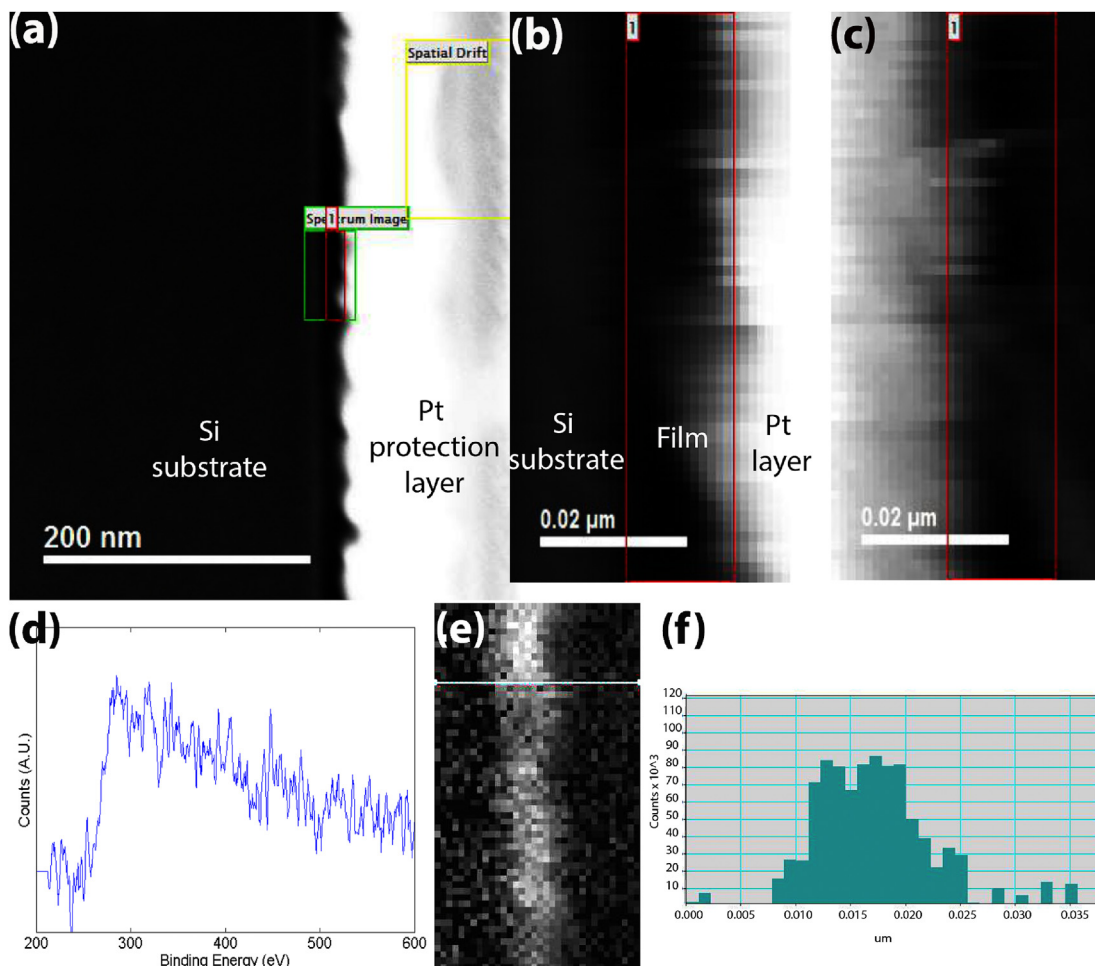


**Fig. 5.** (a) HAADF survey image from film (6) showing target region for EELS spectrum imaging in green and region for spectra sum in red, (b) Magnified HAADF image of target region, (c) spectrum image of the target region in the energy range of the C K-edge, (d) integrated spectra from region highlighted in red after background subtraction, (e) C K-edge distribution in scanned region, (f) Line profile across the scanned region shown by the green line in (e). (A colour version of this figure can be viewed online.)

### 3. Conclusion

Cu covetic PLD films made from a nominally 4 wt% target show uniform integration of carbon within the film for a narrow range of deposition parameters. These films contain up to 19.14 at.% ( $4.1 \pm 0.2$  wt%) C measured by XPS, demonstrating that PLD can transfer significantly more carbon to the film than was possible using e-beam deposition, but some carbon loss still occurs. We show evidence of  $sp^2$  carbon by XPS in PLD Cu covetic films and a peak in the C K-edge in EELS indicative of transitions from  $1s$  to  $\pi^*$  anti-bonding unoccupied state similar to that observed in bulk samples, suggesting that the C transferred retains its graphitic nature, but it is not perfect graphite. The significant increase in C transferred by PLD, compared to e-beam deposition, causes a reduction in oxidation as demonstrated by AFM and the sheet resistance measured over time. This one-step process in the fabrication of a Cu-C alloy thin film that improves oxidation resistance is a step forward in understanding the role that carbon plays when combined with metals and is a promising advancement for more flexible use of Cu-C alloys in nanoelectronics and as transparent conductors.

### 4. Methods

Cu (99.99%) was converted to Cu covetic by adding 4 or 5 wt% C

to Cu by Third Millennium Materials, LLC (e.g. 5 wt% C in Cu is denoted Cu cv 5%). The conversion process involves melting ( $> 1085$  °C) the metal in an induction furnace and stirring in the desired i.e. 5 wt% (21.78 at.%) particles of activated carbon with diameter of  $\leq 50$   $\mu\text{m}$  to the liquid metal. A high DC current,  $\approx 150$  A, is applied to the mixture via graphite electrodes from an arc welder, creating a localized plasma arc [19,28]. The arc initiates a polymerization reaction by ionizing C to  $C^{n+}$  or  $C^{n-}$ . These carbon ions react with each other and with melted copper atoms forming C-C and Cu-C bonds, in a networked structure. The material is allowed to cool in an argon blanket to prevent oxidation. This structure of the Cu-C alloy is preserved under cooling and further re-melting and re-solidification [29–31]. Once solidified, Cu covetic is used as a target for deposition of thin films.

Two deposition techniques were used to deposit copper covetic films: e-beam deposition and pulsed laser deposition (PLD). For e-beam deposition, bulk Cu cv 5% or pure Cu metal, 99.99% (0% C), were used as the target from which material was transferred to Si and glass substrates using a Denton e-beam evaporator. Si purchased from University Wafer was p-type, Boron doped with orientation  $(100) \pm 0.5^\circ$ , thickness 380  $\mu\text{m}$ , and resistance of 1–10 Ohm-cm. Si (111) wafers had similar properties to Si (100), but a lower resistivity of 0.004–0.005 Ohm-cm. The target was placed in a Molybdenum crucible. The chamber was evacuated to a base pressure of  $\approx 5 \times 10^{-6}$  Torr. The current was adjusted such that the

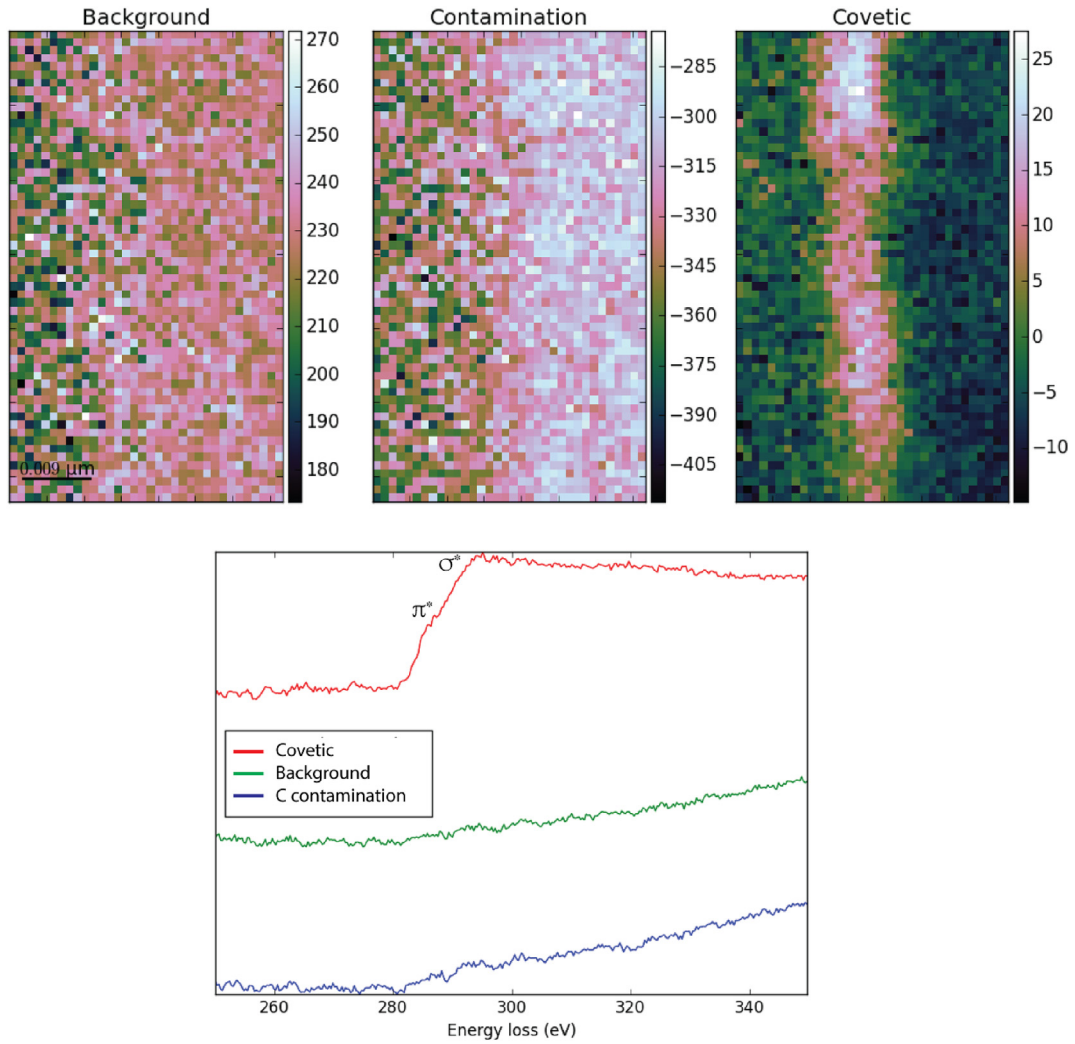


**Fig. 6.** Decomposition of the Spectrum image of film (6) using Blind Source Separation, shows three clear regions in the navigation and signal spaces: background, C contamination and C from the covetic film region. Each component is mapped out in the top images. (A colour version of this figure can be viewed online.)

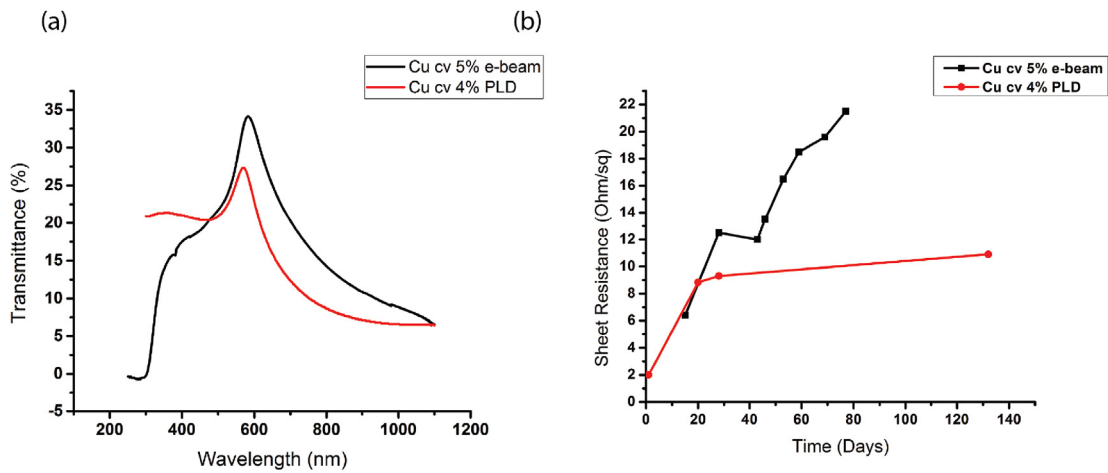


**Fig. 7.** (a) Optical spectroscopy comparing the transmittance of  $\approx 30$  nm Cu cv 5% film made by e-beam deposition and Cu cv 4% film made by PLD, (b) Sheet resistance of the same two films measured over a period of time. (A colour version of this figure can be viewed online.)

evaporation rate was 0.2–0.3 nm/sec.

PLD films were grown using a Blue Wave Semiconductor PLD

system, employing a Quantel Brilliant B solid-state Nd:YAG pulsed laser (400 mJ/pulse @ 532 nm, 10 Hz) at powers ranging from 1.8 –

$3.55W \pm 0.5W$  [32] in an Ar (99.999%) atmosphere with  $\leq 10$  ppb  $O_2$  and  $\leq 20$  ppb  $H_2O$ ,  $\leq 100$  ppb THC,  $\leq 5$  ppb N. Once the base pressure of  $\approx 1 \times 10^{-6}$  Torr was reached, Ar gas was flowed at a rate of 3 sccm, to achieve a deposition pressure of 100 mTorr and the substrate was heated to the desired temperature (150, 350 or 500 °C). The rotating target was ablated for 1 min prior to deposition after which the film was deposited on either Si or sapphire. After the deposition the samples were cooled to room temperature in 100 sccm Ar gas. Films of Cu metal (0% C) were deposited for comparison. Sapphire purchased from Precision Micro-Optic was 99.996% pure, single crystal A-Plane  $(11\bar{2}0) \pm 0.2^\circ$ , double-sided epi-polished, with thickness  $430 \pm 25$   $\mu\text{m}$  and roughness of 0.2 nm.

XRD spectra were measured on a Bruker C2 Discover powder diffractometer using  $CuK\alpha$  radiation from a sealed tube, graphite Gobel mirror with 0.5 mm pinhole collimator, and Vantec500 area detector. Six 2D frames were integrated over 10 min yielding the diffraction spectra from  $2\theta = 10^\circ$  to  $90^\circ$  with steps of  $0.02^\circ$ . XPS was obtained with a Kratos Axis 165 using monochromatic Al (1486.7 eV) X-rays. Survey spectra were collected at a pass energy of 160 eV. High resolution spectra were collected at pass energy of 40 eV and an electron takeoff angle of  $90^\circ$  with respect to the sample surface. The area analyzed by XPS was  $\approx 1$  mm. Depth profiling was done with 4 keV Ar-ions using a rastered area of  $\approx 5$  mm  $\times$  7 mm. XPS detection limits are  $\approx 0.1$  at.%. AFM measurements were made on a Dimension 3000 AFM with Al-coated Si probes with nominal tip radius  $< 10$  nm, natural frequency 110 kHz, and spring constant (K) of 10 N/m. Conductive AFM tests were performed on an Asylum Research Cypher using Rocky Mountain Nanotechnology 25Pt400B solid Pt probes with nominal tip radius  $< 20$  nm, and K of 8 N/m.

Lamella for TEM observation were prepared using a FEI Hellios 650 DualBeam FIB-SEM using Ga ions at 30 kV accelerating voltage after depositing a Pt protective layer. The Ga ion voltage and current were decreased to 5 kV and 15 pA for the final thinning to remove any Ga implantation from previous steps and minimize damage of the electron transparent sample. TEM observation of the copper covet samples was carried out in a JEOL 2100F Field Emission TEM operated at 200 kV with a spherical aberration coefficient of  $C_s = 0.5$  mm, point-point resolution of 0.19 nm and lattice resolution of 0.10 nm. EELS data was acquired in scanning TEM (STEM) mode using a Gatan Tridiem spectrometer with energy resolution of 100 meV. EELS data was analyzed using the multivariate analysis method (MVA). There are several methods to decompose a tensor into several factors; one of the most frequently used is PCA. Decomposition is primarily used to reduce the noise of a dataset or for dimensionality reduction. We assumed a Gaussian distribution of the data and used PCA to denoise data by using a limited set of components (principal) to make a model of the original dataset (spectra). Removing higher order components only has the effect of reducing the noise. Hyperspy decomposes the dataset into a signal space and a navigation space. From these, we were able to resolve the contribution from each component.

UV-VIS data was acquired using a HITACHI U-2910 spectrophotometer, from 300 to 1100 nm with a resolution of 1 nm. The sheet resistance of PLD films was measured in a Signatone S1160 probe station by the van der Pauw method on rectangle-shaped specimens (Keithley 6221 current source and Keithley 2182A nanovoltmeter). The resistivity values were then calculated using film thicknesses measured by preparing cross-sections in the dual beam FIB-SEM and measured in the TEM.

## References

- [1] N.F. Mott, Oxidation of metals and the formation of protective films, *Nature* 6 (1940) 996–1000.

- [2] J.P. Baur, D.W. Bridges, W.M. Fassell, Oxidation of oxygen-free high conductivity copper to  $Cu_2O$ , *J. Electrochem. Soc.* 103 (5) (1956) 273, <http://dx.doi.org/10.1149/1.2430310>.
- [3] D.W. Bridges, J.P. Baur, G. Baur, W.M. Fassell, Oxidation of copper to  $Cu_{20}$  and  $CuO$ , *J. Electrochem. Soc.* 103 (9) (1956) 475–478.
- [4] H. Guo, N. Lin, Y. Chen, Z. Wang, Q. Xie, T. Zheng, N. Gao, S. Li, J. Kang, D. Cai, D.-L. Peng, Copper nanowires as fully transparent conductive electrodes, *Sci. Rep.* 3 (2013) 2323, <http://dx.doi.org/10.1038/srep02323>. <http://www.pubmedcentral.nih.gov/articlerender.fcgi?artid=3728602&tool=pmcentrez&rendertype=abstract>.
- [5] P.-C. Hsu, H. Wu, T.J. Carney, M.T. McDowell, Y. Yang, E.C. Garnett, M. Li, L. Hu, Y. Cu, Passivation coating on electrospun copper nanofibers for stable transparent electrodes, *ACS Nano* 6 (6) (2012) 5150–5156.
- [6] A.R. Rathmell, S.M. Bergin, Y.-L. Hua, Z.-Y. Li, B.J. Wiley, The growth mechanism of copper nanowires and their properties in flexible, transparent conducting films, *Adv. Mater.* 22 (32) (2010) 3558–3563, <http://dx.doi.org/10.1002/adma.201000775>. <http://www.ncbi.nlm.nih.gov/pubmed/20512817>.
- [7] V.M. Kozhevnikov, D.A. Yavsin, I.P. Smirnova, M.M. Kulagina, S.A. Gurevich, Effect of oxidation on the electrical properties of granular copper nanostructures, *Phys. Solid State* 45 (10) (2003) 1993–2000, <http://dx.doi.org/10.1134/1.1620108>.
- [8] M. Lin, L.C.L. Chen, J. Lee, H. Liu, C. Chou, K. Wan, H. Chen, K. Chou, R. Hsiao, E. Lin, A New IC interconnection scheme and design architecture for high performance ICs at very low fabrication cost - post passivation interconnection, in: Proceedings of the IEEE 2003 Custom Integrated Circuits Conference, 2003, 2003, pp. 533–536, <http://dx.doi.org/10.1109/CICC.2003.1249454>.
- [9] D.S. Hecht, L. Hu, G. Irvin, Emerging transparent electrodes based on thin films of carbon nanotubes, graphene, and metallic nanostructures, *Adv. Mater.* 23 (13) (2011) 1482–1513, <http://dx.doi.org/10.1002/adma.201003188>. <http://www.ncbi.nlm.nih.gov/pubmed/21322065>.
- [10] S.-K. Lee, H.-C. Hsu, W.-H. Tuan, Oxidation behavior of copper at a temperature below 300 C and the methodology for passivation, *Mater. Res.* 19 (1) (2016) 51–56, <http://dx.doi.org/10.1590/1980-5373-MR-2015-0139>. [http://www.scielo.br/scielo.php?script=sci\\_arttext&pid=S1516-14392016000100051&lng=en&nrm=iso&tlng=en](http://www.scielo.br/scielo.php?script=sci_arttext&pid=S1516-14392016000100051&lng=en&nrm=iso&tlng=en).
- [11] J. Tian, H. Cao, W. Wu, Q. Yu, N.P. Guisinger, Y.P. Chen, Graphene induced surface reconstruction of Cu, *Nano Lett.* 12 (8) (2012) 3893–3899, <http://dx.doi.org/10.1021/nl3002974>. <http://www.ncbi.nlm.nih.gov/pubmed/22803962>.
- [12] I. Forbeaux, J.-M. Themlin, J.-M. Debever, Heteroepitaxial graphite on 6H-SiC(0001): interface formation through conduction-band electronic structure, *Phys. Rev. B* 58 (24) (1998) 16396–16406, <http://dx.doi.org/10.1103/PhysRevB.58.16396>.
- [13] J. Hass, R. Feng, T. Li, X. Li, Z. Zong, W.A. de Heer, P.N. First, E.H. Conrad, C. A. Jeffrey, C. Berger, Highly ordered graphene for two dimensional electronics, *Appl. Phys. Lett.* 89 (14) (2006) 143106, <http://dx.doi.org/10.1063/1.2358299>. <http://link.aip.org/link/APPLAB/v89/i14/p143106/s1&Agg=doi>.
- [14] C. Riedel, C. Coletti, U. Starke, Structural and electronic properties of epitaxial graphene on SiC(0001): a review of growth, characterization, transfer doping and hydrogen intercalation, *J. Phys. D Appl. Phys.* 43 (37) (2010) 374009, <http://dx.doi.org/10.1088/0022-3727/43/37/374009>. <http://stacks.iop.org/0022-3727/43/i=37/a=374009?key=crossref>. <http://arxiv.org/abs/1508.00001>.
- [15] S. Iijima, Helical microtubules of graphitic carbon, *Nature* 354 (6348) (1991) 56–58, <http://dx.doi.org/10.1038/354056a0>.
- [16] S. Iijima, T. Ichihashi, Single-shell carbon nanotubes of 1-nm diameter, *Nature* 363 (6430) (1993) 603–605, <http://dx.doi.org/10.1038/363603a0>.
- [17] A. Raychowdhury, K. Roy, Modeling of metallic carbon-nanotube interconnects for circuit simulations and a comparison with Cu interconnects for scaled technologies, *IEEE Trans. Computer Aided Des. Integr. Circuits Syst.* 25 (1) (2006) 58–65, <http://dx.doi.org/10.1109/TCAD.2005.853702>.
- [18] K. Subramaniam, T. Yamada, K. Kobashi, A. Sekiguchi, D.N. Futaba, M. Yumura, K. Hata, One hundred fold increase in current carrying capacity in a carbon nanotube-copper composite, *Nat. Commun.* 4 (2013) 2202, <http://dx.doi.org/10.1038/ncomms3202>. <http://www.pubmedcentral.nih.gov/articlerender.fcgi?artid=3759037&tool=pmcentrez&rendertype=abstract>.
- [19] Shugart J, Scherer R. Copper Carbon Composition. US Patent No: 2013/0062572 A2; 2013.
- [20] G.A. López, E.J. Mittemeijer, The solubility of C in solid Cu, *Scr. Mater.* 51 (1) (2004) 1–5, <http://dx.doi.org/10.1016/j.scriptamat.2004.03.028>. <http://linkinghub.elsevier.com/retrieve/pii/S1359646204001769>.
- [21] R.A. Isaacs, H. Zhu, C. Preston, A. Mansour, M. Lemieux, P.Y. Zavalij, H.M.I. Jaim, O. Rabin, L. Hu, L.G. Salamanca-Riba, Nanocarbon-copper thin film as transparent electrode, *Appl. Phys. Lett.* 106 (193108) (2015), <http://dx.doi.org/10.1063/1.4921263>.
- [22] R. Jordan, D. Cole, G. Lunney, K. Mackay, D. Givord, J. Lunney, Pulsed laser ablation of copper, *Appl. Surf. Sci.* 86 (1–4) (1995) 24–28, [http://dx.doi.org/10.1016/0169-4332\(94\)00370-X](http://dx.doi.org/10.1016/0169-4332(94)00370-X). <http://linkinghub.elsevier.com/retrieve/pii/016943329400370X>.
- [23] A. Mesli, T. Heiser, E. Mulheim, Copper diffusivity, Silicon A Re-examination, *Mater. Sci. Eng. B* 25 (2–3) (1994) 141–146, [http://dx.doi.org/10.1016/0921-5107\(94\)90215-1](http://dx.doi.org/10.1016/0921-5107(94)90215-1).
- [24] Y. Zhu, K. Mimura, M. Isshiki, Oxidation mechanism of  $Cu_2O$  to  $CuO$  at 600–1050 C, *Oxid. Metals* 62 (3–4) (2004) 207–222, <http://dx.doi.org/10.1007/s11085-004-7808-6>.

- [25] K. Mimura, J.-W. Lim, M. Isshiki, Y. Zhu, Q. Jiang, Brief review of oxidation kinetics of copper at 350 C to 1050 C, *Metall. Mater. Trans. A* 37 (4) (2006) 1231–1237, <http://dx.doi.org/10.1007/s11661-006-1074-y>.
- [26] F. de la Pena, M. Walls, M. Sarahan, T. Ostasevicius, S. Mazzucco, A. Eljarrat, P. Burdet, J. Taillon, G. Donval, V.T. Fauske, M. Nord, L.F. Zagonel, *Iygr. Hyperspy: HyperSpy 0.8.2*, Aug 2015, <http://dx.doi.org/10.5281/zenodo.28025>. <http://zenodo.org/record/28025>.
- [27] F. de la Pena, M.H. Berger, J.F. Hochepeid, F. Dynys, O. Stephan, M. Walls, Mapping titanium and tin oxide phases using EELS: an application of independent component analysis, *Ultramicroscopy* 111 (2) (2011) 169–176, <http://dx.doi.org/10.1016/j.ultramic.2010.10.001>.
- [28] Shugart JV, Scherer RC. Metal-Carbon Compositions. US 2012/0009110 A1; 2012.
- [29] L.G. Salamanca-Riba, R.A. Isaacs, M.C. LeMieux, J. Wan, K. Gaskell, Y. Jiang, M. Wuttig, A.N. Mansour, S.N. Rashkeev, M.M. Kuklja, P.Y. Zavalij, J.R. Santiago, L. Hu, Synthetic crystals of silver with carbon: 3D epitaxy of carbon nanostructures in the silver lattice, *Adv. Funct. Mater.* 25 (30) (2015) 4768–4777, <http://dx.doi.org/10.1002/adfm.201501156>.
- [30] H.I. Jaim, R.A. Isaacs, S.N. Rashkeev, M. Kuklja, D.P. Cole, M.C. LeMieux, I. Jasiuk, S. Nilufar, L.G. Salamanca-Riba, Sp<sup>2</sup> Carbon Embedded In Al-6061 and Al-7075 alloys in the form of crystalline graphene nanoribbons, *Carbon* 107 (2016) 56–66, <http://dx.doi.org/10.1016/j.carbon.2016.05.053>. <http://linkinghub.elsevier.com/retrieve/pii/S0008622316304195>.
- [31] H.I. Jaim, D.P. Cole, L.G. Salamanca-Riba, Characterization of carbon nanostructures in Al and Ag covetic alloys, *Carbon* 111 (2017) 309–321, <http://dx.doi.org/10.1016/j.carbon.2016.10.007>. <http://linkinghub.elsevier.com/retrieve/pii/S0008622316308661>.
- [32] J.E. Cornett, O. Rabin, Pulsed laser deposition and annealing of Bi(2-x)SbxTe<sub>3</sub> thin films for p-type thermoelectric elements, *Solid-State Electron.* 101 (2014) 106–115, <http://dx.doi.org/10.1016/j.sse.2014.06.018>. <http://linkinghub.elsevier.com/retrieve/pii/S0038110114001518>.